

Scalable and efficient Sb₂S₃ thin-film solar cells fabricated by close space sublimation

Cite as: APL Mater. **7**, 041105 (2019); <https://doi.org/10.1063/1.5090773>

Submitted: 29 January 2019 . Accepted: 18 March 2019 . Published Online: 04 April 2019

Liping Guo, Baiyu Zhang, Shan Li, Qian Zhang , Michael Buettner, Lin Li, Xiaofeng Qian , and Feng Yan 



View Online



Export Citation



CrossMark

ARTICLES YOU MAY BE INTERESTED IN

[The growth and phase distribution of ultrathin SnTe on graphene](#)

APL Materials **7**, 041102 (2019); <https://doi.org/10.1063/1.5091546>

[Reactions at noble metal contacts with methylammonium lead triiodide perovskites: Role of underpotential deposition and electrochemistry](#)

APL Materials **7**, 041103 (2019); <https://doi.org/10.1063/1.5083812>

[Tunable perpendicular magnetic anisotropy in epitaxial Y₃Fe₅O₁₂ films](#)

APL Materials **7**, 041104 (2019); <https://doi.org/10.1063/1.5090292>



Measure Ready
M91 FastHall™ Controller

A revolutionary new instrument
for complete Hall analysis

 Lake Shore
CRYOTRONICS

Scalable and efficient Sb_2S_3 thin-film solar cells fabricated by close space sublimation

Cite as: APL Mater. 7, 041105 (2019); doi: 10.1063/1.5090773

Submitted: 29 January 2019 • Accepted: 18 March 2019 •

Published Online: 4 April 2019



Liping Guo,^{1,a)} Baiyu Zhang,^{2,a)} Shan Li,³ Qian Zhang,³  Michael Buettner,⁴ Lin Li,¹ Xiaofeng Qian,^{2,b)} 
and Feng Yan^{1,4,b)} 

AFFILIATIONS

¹Department of Metallurgical and Materials Engineering, The University of Alabama, Tuscaloosa, Alabama 35487, USA

²Department of Materials Science and Engineering, Texas A&M University, College Station, Texas 77843, USA

³Department of Materials Science and Engineering, Harbin University of Technology, Shenzhen 518055, China

⁴Centre for Materials for Information Technology, The University of Alabama, Tuscaloosa, Alabama 35487, USA

^{a)}Contributions: L. Guo and B. Zhang contributed equally to this work.

^{b)}Authors to whom correspondence should be addressed: fyan@eng.ua.edu and feng@tamu.edu

ABSTRACT

Antimony sulfide as a cost-effective, low-toxic, and earth-abundant solar cell absorber with the desired bandgap was successfully deposited using a scalable close space sublimation technique. The deposition process can separately control the substrate and source temperature with better engineering of the absorber quality. The device performance can reach 3.8% with the configuration of glass/FTO/CdS/ Sb_2S_3 /graphite back contact. The defect formation energy and the corresponding transition levels were investigated in detail using theoretical calculations. Our results suggest that Sb_2S_3 exhibits intrinsic *p*-type owing to S-on-Sb antisites (S_{Sb}) and the device performance is limited by the S vacancies. The localized conduction characterization at nanoscale shows that the non-cubic Sb_2S_3 has conductive grains and benign grain boundaries. The study of the defects, microstructure, and nanoscale conduction behavior suggests that Sb_2S_3 could be a promising photovoltaic candidate for scalable manufacturing.

© 2019 Author(s). All article content, except where otherwise noted, is licensed under a Creative Commons Attribution (CC BY) license (<http://creativecommons.org/licenses/by/4.0/>). <https://doi.org/10.1063/1.5090773>

Solar cells convert solar energy directly into electricity and provide one of the most effective ways to generate renewable, sustainable, and affordable energy.^{1,2} Recently, a group of non-cubic chalcogenide photovoltaics shed light on the potential thin film solar cell application.^{3–5} The orthorhombic Sb_2Se_3 thin film solar cell can achieve power conversion efficiency (PCE) up to 7.6% with inexpensive low-temperature evaporations, e.g., vapor transport deposition (VTD), demonstrating the great potential of these materials.^{6–10} Compared to the low bandgap of antimony selenide Sb_2Se_3 (i.e., 1.1 eV), antimony sulfide Sb_2S_3 possesses a wide bandgap of ~1.7 eV, as well as desired photovoltaic behavior.^{11,12} The Sb_2S_3 solar cells with the solution-based process with PCE of ~7.5% have also been achieved.¹³ These materials exhibit unique crystal structures with quasi-one-dimensional ribbons bonded by weak van der Waals force, e.g., $(\text{Sb}_4\text{X}_6)_n$ ribbons in Sb_2X_3 ,¹⁴ where X = (Se, S). The ribbon-like morphologies lead to

highly anisotropic charge transport, different from traditional cubic solar cell materials with isotropic transport (e.g., CdTe, CIGS, and perovskites).^{3,8,15}

To date, a variety of growth technologies have been developed for Sb_2S_3 film deposition to achieve high-quality absorber with the ribbons aligned with the buffer layer for desired charge transport.³ For example, Sb_2S_3 solar cells can achieve PCE of 3.5% with rapid thermal evaporation (RTE).^{15–18} Recently, high efficiency Sb_2S_3 solar cells using the solution-based process were reported. For instance, sensitized solar cells have PCE of 6.4% using a solution-based technology^{18–20} and solution processing for highly efficient Sb_2S_3 with PCE of 6.78%–7.5% with varying starting precursors.⁵ Sb_2S_3 solar cells fabricated by atomic layer deposition (ALD) in planar structure can achieve PCE of ~5.7%.²¹ However, it is highly desired to employ the physical vapor deposition technologies to integrate the Sb_2S_3 into the commercial thin-film solar cell manufacturing.

In particular, fast deposition techniques with independent control of the substrate and source temperature are highly demanded for integrating Sb_2S_3 into the high-throughput manufacturing technology. The close space sublimation (CSS) process is well known for CdTe manufacturing which directly vaporizes the solid source materials and allows high-throughput deposition on moving substrates.^{10,22,23} The CSS technique can greatly reduce the cost and improve the absorber quality.¹⁴ Recently, the CSS technology has been successfully applied to Sb_2Se_3 thin film solar cells with PCE of 6.8%.^{14,24}

In this work, we experimentally investigated the Sb_2S_3 growth and the performance of CSS-grown Sb_2S_3 solar cells. It is demonstrated that Sb_2S_3 can be successfully grown using the CSS technique. The best device performance is 3.8% PCE. A theoretical study based on first-principles density functional theory (DFT)^{25,26} was performed to elucidate its electronic and optical property. In addition, the study of intrinsic point defects and deep energy states provides a deeper understanding of the device performance. Our work further paves the way of antimony chalcogenide based emerging cost-effective and earth-abundant thin-film photovoltaics for solar energy applications.

About 60-nm thick CdS window layers were deposited on a cleaned fluorine-doped SnO_2 coated soda-lime glass (FTO TEC 10, Pilkington, USA) by chemical bath deposition (CBD) at a bath temperature of 65 °C. The CdS films were annealed in air at 400 °C for 30 min to improve the crystallization with CdCl_2 solution treatment. Sb_2S_3 thin films were grown in Ar ambient using a commercial CSS system (MTI, USA). The high purity Sb_2S_3 powder (99.999%, Alfa Aesar, USA) was placed on the bottom AlN plate, and the CdS coated FTO substrate was loaded on the top AlN plate (10 mm distance from the Sb_2S_3 powder). To optimize the growth conditions of Sb_2S_3 absorbers, the substrate and source temperatures were varied from 300 °C to 400 °C and 500 °C to 580 °C, respectively, at chamber base pressure about 5 mTorr, and the deposition pressure is about 15 mTorr. The Sb_2S_3 thin film thickness can be tuned by varying the deposition time from 30 to 100 s, then switching off the halogen lamp heater, and cooling the film naturally to room temperature. The as-grown Sb_2S_3 films were rinsed with de-ionized water, and then graphite and Ag paste was screen printed on the Sb_2S_3 (with an active area of 0.08 cm²) to define the solar cells. The finished solar cell's current-voltage (*J-V*) curve was characterized using a solar simulator (Newport, Oriel Class AAA 94063A, 1000 W xenon light source) with a source meter (Keithley 2420) at 100 mW/cm² AM 1.5G irradiation. A calibrated Si-reference cell and meter (Newport, 91150 V, certificated by NREL) was used to calibrate the solar simulator before each measurement. The external quantum efficiency (EQE) data were obtained by using a solar cell spectral response measurement system (QE-T, Enli Technology, Co., Ltd). The film thickness was determined by using the surface profilometer (Dektak V220). The structure of the grown films was characterized by using an X-ray diffraction (XRD) system (X'Pert). The film morphologies and chemical composition were determined by using the scanning electron microscope (SEM, JEOL 7000) with Electron-dispersive Spectroscopy (EDS) attached to the SEM. The Raman experiments were conducted on a single stage Raman spectrometer with a solid-state laser (Horiba LabRam HR, 532 nm wavelength). The absorbance and transmittance spectra were measured using a UV-Vis spectrometer (Shimadzu

UV-1800). The atomic force microscopy (AFM) and conductive AFM images were recorded on a grounded Sb_2S_3 sample using atomic force microscopy (AFM, Park XE70). The topography and current images were simultaneously recorded in contact mode using a Pt/Ir coated contact probe (ANSCM-PT from AppNano, Inc.). The cantilever spring constant was about 3 N/m, and resonance frequency was ~60 kHz.

Atomistic, electronic structures and optical properties of Sb_2S_3 crystals were calculated using first-principles DFT^{25,26} as implemented in the Vienna *Ab Initio* Simulation Package (VASP).²⁷ The Perdew-Burke-Ernzerhof (PBE)²⁸ form of exchange-correlation functional within the generalized gradient approximation (GGA)²⁹ and a plane wave basis set with a 400 eV energy cutoff were employed for VASP calculations. To account for van der Waals (vdW) interactions between $(\text{Sb}_4\text{S}_6)_n$ ribbons, we adopted optB86-vdW functional.^{30–32} The structural optimization and electronic relaxation were calculated in a Γ -centered Monkhorst-Pack³³ k-point sampling grid of $4 \times 12 \times 4$. The maximal residual force of each atom is less than 0.01 eV Å⁻¹, and the convergence criterion for electronic relaxation was set to 10⁻⁶ eV. As the DFT-GGA often underestimates the bandgap, we adopt the modified Becke-Johnson (MBJ)³⁴ exchange potential and hybrid HSE06 functional³⁵ for electronic structure and optical property calculations. We used a $12 \times 28 \times 12$ k-point grid in the MBJ calculations and $3 \times 9 \times 3$ k-point grid in the HSE06 calculations. The MBJ calculation yields a bandgap close to the HSE06 result for Sb_2S_3 . For the defect calculations, we increase the supercell by $2 \times 6 \times 2$ which contains 480 atoms and apply an energy correction scheme which includes potential alignment and image-charge correction. There is a trade-off between computational cost and errors caused by the finite-size effect.^{36,37} We checked the cell-dependent defect formation energies and found that the error caused by the finite-size effect is large in the $1 \times 3 \times 1$ supercell but becomes much smaller in the $2 \times 6 \times 2$ supercell, suggesting that it is necessary to employ a large supercell. The cutoff energy for defect calculations is set to 300 eV. More details of the calculations and methods can be seen in the [supplementary material](#).

Since Sb_2S_3 has a low melting point ($T_m \sim 550$ °C) and high vapor pressure, we deposit Sb_2S_3 with a relative lower source temperature than that for Sb_2Se_3 ($T_m \sim 608$ °C).³⁸ As shown in Fig. 1(a), the XRD spectrum for the Sb_2S_3 film was indexed as orthorhombic structure with Pbnm space group, with respect to the Joint Committee for Powder Diffraction Standards (JCPDS) 42-1393.³⁹ The as-grown Sb_2S_3 film displays strong (211)-preferred orientation. The substrate temperature during the growth significantly impacts the orientation of the Sb_2Se_3 due to its orthorhombic crystalline structure, which is similar to the previous report.¹⁶ This (211)-preferred orientation can benefit charge transfer along the $(\text{Sb}_4\text{S}_6)_n$ ribbons, like the $(\text{Sb}_4\text{Se}_6)_n$ ribbons in Sb_2Se_3 film.^{8,14} The Raman spectrum is shown in Fig. 1(b), suggesting a good crystallinity. The two major peaks located at 139 and 292 cm⁻¹ are ascribed to the Sb and symmetric vibrations of Sb_2S_3 pyramidal units with C_{3v} symmetry, respectively.^{40,41} Other weak Raman peaks are indexed at 184 and 247 cm⁻¹. To understand the Sb_2S_3 electronic structure, Figs. 1(d) and S1 show the calculated electronic structure and orbital-resolved projected density of state (PDOS) using first-principles DFT with MBJ³⁴ and HSE06 functional³⁵ (calculation details can be found in the [supplementary material](#)). The PDOS indicates that the valence band is dominated by S-*p* orbitals, and the

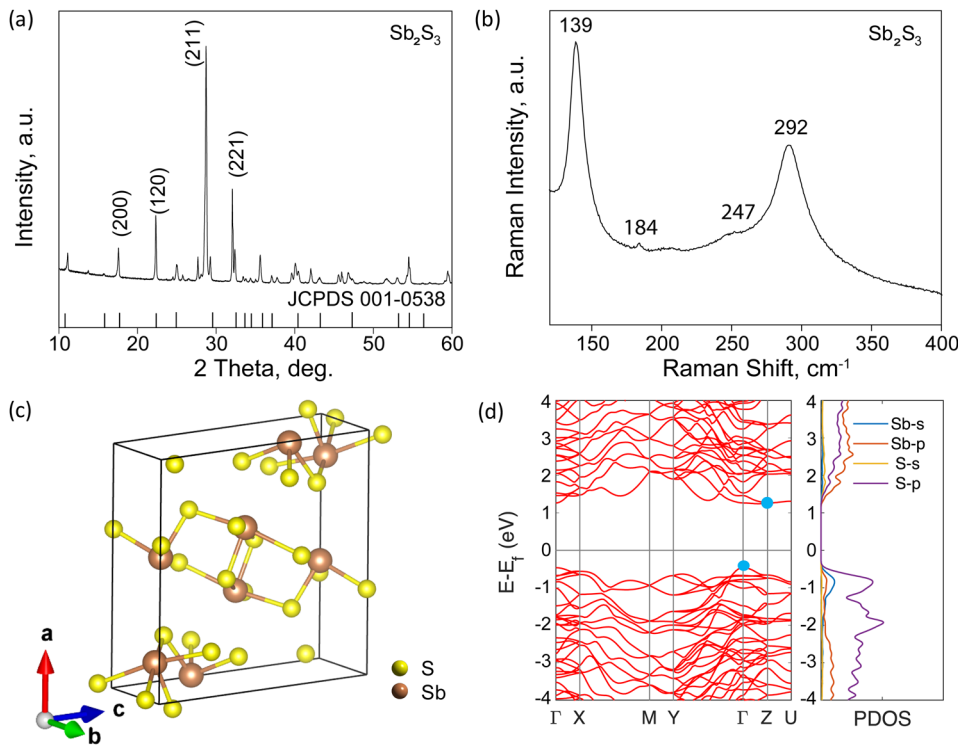


FIG. 1. Crystal and electronic structure of CSS-grown Sb_2S_3 . (a) XRD patterns for the Sb_2S_3 film deposited with a thickness of 600 nm. The standard Sb_2S_3 structure is plotted at the bottom using JCPDS No. 42-1393 as reference. (b) Raman analysis for the Sb_2S_3 film. (c) Atomic configuration with the Pnma space group and (d) electronic structure and orbital-resolved projected density of state (PDOS) of Sb_2S_3 with bandgap ~ 1.7 eV, calculated by DFT with MBJ + vdW functionals.

conduction band is dominated by Sb-*p* and Sb-*s* orbitals. Moreover, the DFT-MBJ results predicted that the indirect and direct bandgaps of Sb_2S_3 are 1.71 and 1.74 eV, respectively, which agree with the experimental optical bandgap (1.56 and 1.71 eV; see more details later).

Figure 2(a) shows the top view of the as-grown Sb_2S_3 film, indicating a dense and pin-hole free morphology with polyhedron grains. The grain size distribution is non-uniform with some

extremely large grains ($\sim 1 \mu\text{m}$) and some small grains (~ 300 nm). This may be due to the fast deposition process during the CSS deposition ($\sim 1 \mu\text{m}\cdot\text{min}^{-1}$). The cross-sectional image as shown in Fig. 2(b) indicates that the Sb_2S_3 thickness is ~ 400 nm with a 50 nm CdS layer. The chemical composition was determined using the energy dispersive X-ray spectroscopy (EDS), as shown in the inset of Fig. 2(b), where the atomic ratio between S and Sb is 60.4:39.6, close to the stoichiometry of 3:2 in Sb_2S_3 . The chemical distribution across

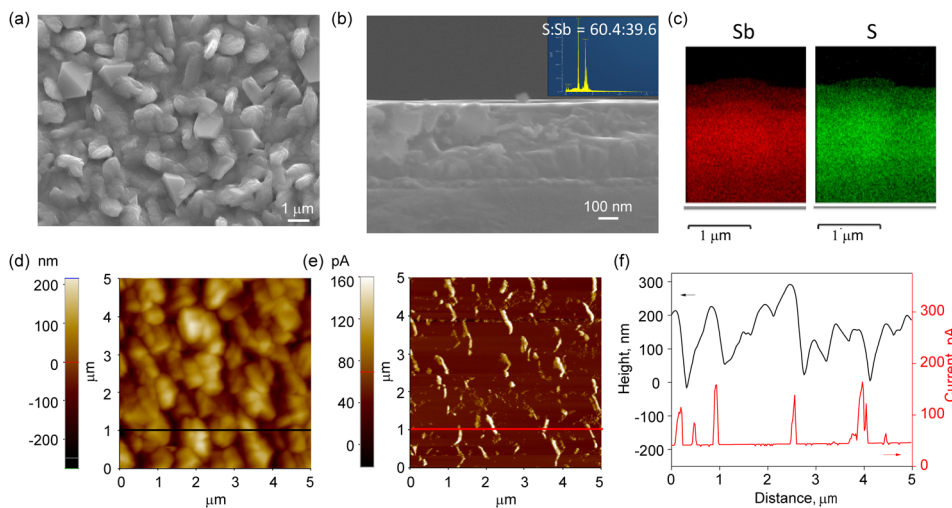


FIG. 2. Microstructure, chemical composition, and nanoscale conductivity of the CSS grown Sb_2S_3 film. (a) Top view of the scanning electron microscopy (SEM) image; (b) cross-sectional view of the SEM image; inset of (b) energy dispersive spectroscopy (EDS) spectra. EDS spectra of the Sb_2S_3 film with detected elements S and Sb in a ratio of $\sim 3:2$. (c) EDS elemental mapping of the corresponding cross-sectional Sb_2S_3 . (d) Atomic force microscopy (AFM) image and (e) conductive atomic force microscopy (cAFM). (f) The correlation between topography and conductivity of grains and grain boundaries was determined by the current and height difference shown in (d) and (e) indexed by the dashed line. The AFM and cAFM scanning area is $5.0 \times 5.0 \mu\text{m}^2$.

the film is characterized using EDS mapping, as shown in Fig. 2(c), where the Sb and S elements distributed uniformly without segregation. To ascertain the uniformity of the grain size and the localized conductivity, we performed additional characterization using the atomic force microscopy (AFM) and conductive AFM (cAFM), as shown in Figs. 2(d)–2(f). The topography and current images are $5 \times 5 \mu\text{m}^2$. The conductive AFM image was measured with a sample bias of +6 V. The line profile for the topography height and conductivity in Fig. 2(f) shows that the grain boundary area (valley in the height profile) has a higher resistivity while the grain (peak of the height profile) is more conductive, in line with the observation in Sb_2Se_3 but very different from other cubic photovoltaic materials such as CdTe.¹⁴ This is possibly due to the $(\text{Sb}_4\text{S}_6)_n$ ribbons grown perpendicular to the substrate, where their vdW boundaries without dangling bonds suppress carrier recombination at the grain boundaries.

The optical absorption properties were characterized using UV-Vis spectroscopy, as shown in Fig. 3(a), where the strong absorption edge starting around 750 nm can also be observed in the transmittance plot [Fig. 3(b)]. The direct and indirect bandgaps can be determined as 1.71 and 1.56 eV by extracting the Tauc fitting, as shown in Fig. 3(c) and the inset. The experimental direct bandgap is in good agreement with the theoretical calculation, as shown in Table S2. Figure 3(d) and the inset are the calculated absorption coefficients of Sb_2S_3 compared with Sb_2Se_3 . It is shown that both materials exhibit excellent light absorption, while Sb_2S_3 shows slightly better absorption than that of Sb_2Se_3 in a higher energy

range. Overall, the optical absorption calculation demonstrates that Sb_2S_3 is a promising absorber material for non-cubic chalcogenide solar cells.

To elucidate the surface state of the CSS grown Sb_2S_3 film, the X-ray photoelectron spectroscopy (XPS) measurement was performed, and the results are shown in Fig. 4. The binding energies (BE) of all the peaks were corrected with C1s energy at 284.6 eV. The full spectrum survey is given in Fig. 4(a), showing the presence of Sb 3d and S 2p peaks. The high-resolution XPS spectra of Sb 3d are displayed in Fig. 4(b) with peaks at 539.9 eV for Sb 3d_{3/2}, and 532 eV for Sb 3d_{5/2}, respectively. These two peaks correspond to Sb³⁺ oxidation states in Sb_2S_3 . In the high-resolution S2p spectrum, four peaks were observed at 161.5, 163.1, 164.0, and 165.2 eV, respectively. These peaks correspond to the S 2p_{3/2} and S 2p_{1/2}, as shown in Fig. 4(c).

The Sb_2S_3 solar cell was fabricated in an FTO/CdS/ Sb_2S_3 /graphite cell structure, as shown in Fig. 5(a), and their device performance was measured accordingly. Figures 5(b) and 5(c) show the energy level alignment and the current-voltage (*J*-*V*) curve, and the external quantum efficiency (EQE) of the device, respectively. The typical device performance is listed in Table I. The best device performance is 3.83% with the open circuit voltage of 0.66 V, short circuit current density (*J*_{sc}) of $\sim 13 \text{ mA cm}^{-2}$, and Fill Factor (FF) of $\sim 44.65\%$. Therefore, the CSS-grown Sb_2S_3 film device performance is on par with the thermal evaporation deposited Sb_2S_3 solar cells, though still lower than that of the dye-sensitized solar cells.^{12,13,15,21,38}

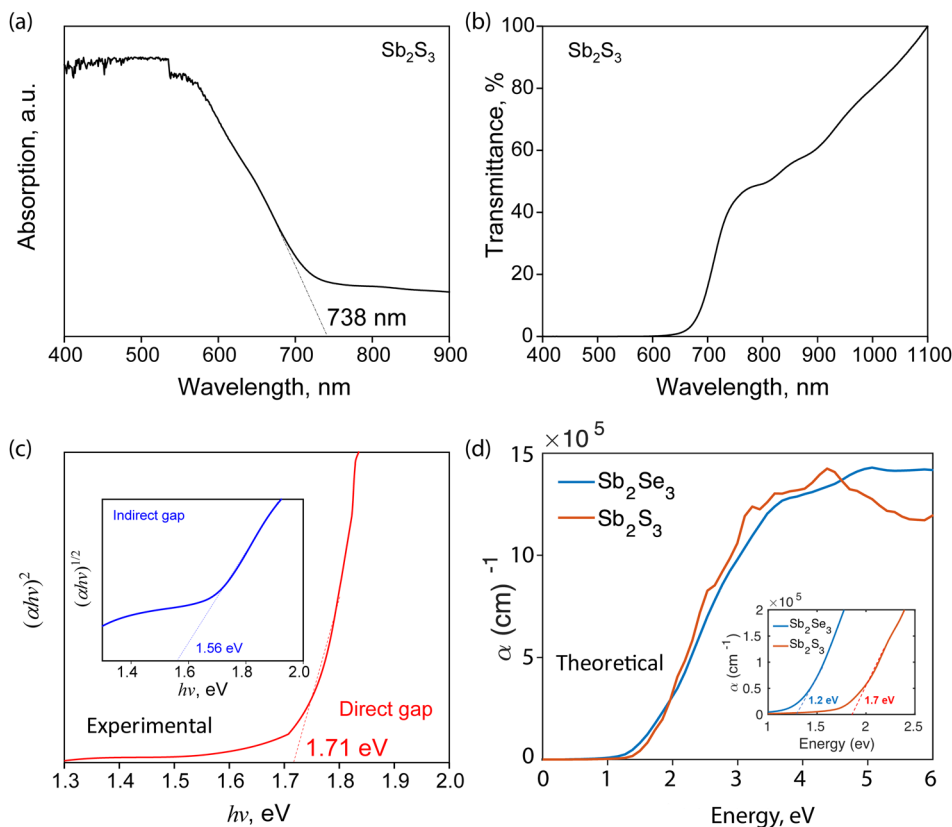


FIG. 3. The experimental and theoretical optical properties of the CSS grown Sb_2S_3 film. [(a) and (b)] The absorbance and transmittance spectrum of the Sb_2S_3 with (c) the direct and indirect bandgaps extracted from the optical spectra, respectively. (d) Calculated optical absorption coefficients of Sb_2Se_3 and Sb_2S_3 .

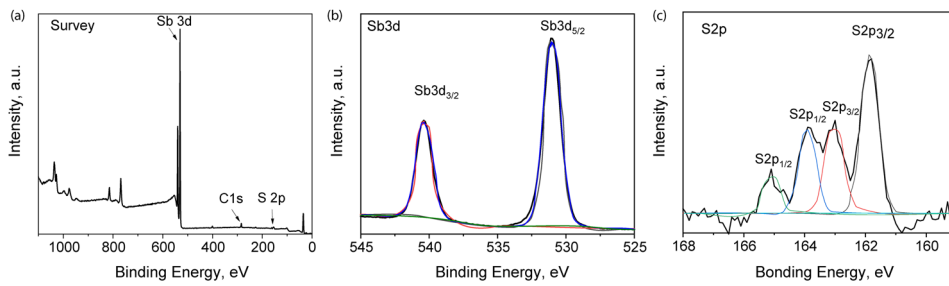


FIG. 4. XPS of the CSS grown Sb_2S_3 film. (a) Survey XPS spectra, (b) Sb 3d, and (c) S 2p for the as-grown Sb_2S_3 film.

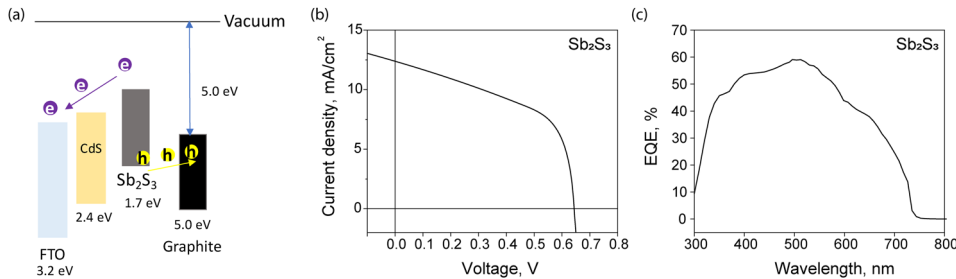


FIG. 5. Device performance of the Sb_2S_3 cells. (a) illustrative energy level diagram of the layers in the cells; [(b) and (c)] the current density-voltage (J-V curve) and EQE spectra of the orientation-dependent films.

TABLE I. Sb_2S_3 solar cell device performance parameters of the champion device grown by CSS.

V_{oc} (V)	J_{sc} (mA cm^{-1})	FF (%)	R_s ($\Omega \text{ cm}^2$)	R_{sh} ($\Omega \text{ cm}^2$)	PCE (%)
0.66	13.0	44.65	129.25	1787	3.83

To understand the defect chemistry inside the CSS deposited Sb_2S_3 , we perform first-principles defect formation energy calculations. Here, we consider five types of intrinsic defects, including Sb vacancy (V_{Sb}), S vacancy (V_{S}), S interstitial (S_{i}), and Sb and S antisites (Sb_{S} and S_{Sb}), and the calculation details can be found in the [supplementary material](#). Figures 6(a) and 6(b) show the formation energy of each defect type under S-rich and S-poor condition, respectively, and Fig. 6(c) shows the corresponding transition levels of charged defects. As shown in Fig. 6(c), V_{Sb} , S_{i} , and Sb_{S} are p -type defects (labeled in red); V_{S} and Sb_{S} are n -type defects (labeled in blue). Only V_{Sb} and Sb_{S} show relatively shallow acceptor levels (0/-1), i.e., transition levels located near valence band maximum

(VBM). The ionization energy of these two levels is located at ~ 0.07 eV and ~ 0.28 eV, respectively. However, the formation energy of Sb vacancy is relatively high, which is above 2 eV in S rich condition, while S_{Sb} has a formation energy of ~ 1 eV, much lower than V_{Sb} . Thus, S_{Sb} is potentially the dominant defect type in Sb_2S_3 that contributes to the p -type conduction. As for the n -type defects, V_{S} exhibits a rather deep donor level (2/0) far below the conduction band minimum (CBM), indicating that it is difficult to ionize, thus rarely contributing to n -type conductivity. In addition, Sb_{S} shows the n -type transition level (~ 0.2 eV); nevertheless, it is unlikely to form in the S-rich condition due to its high formation energy above 2 eV. Overall, Sb_2S_3 exhibits p -type conductivity and S_{Sb} is the dominant native acceptor defect species. The loss of S will lead to the low device performance by diminishing Sb_2S_3 intrinsic p -typeness because V_{S} and Sb_{S} have lower formation energy, while V_{Sb} has higher formation energy in S-poor condition, compared to the S-rich condition. The calculation results are in agreement with the previous report.⁴² These observations are similar to the defect study of the Sb_2Se_3 system.⁴³ In summary, the intrinsic p -type conductivity of Sb_2S_3 originates from S_{Sb} , and the S chemical potential significantly

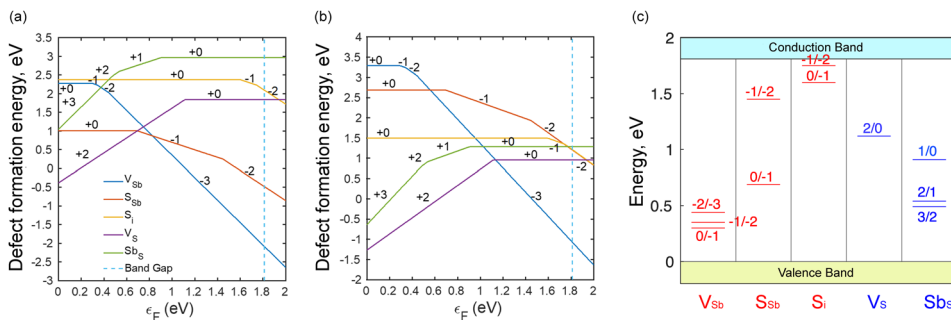


FIG. 6. Defect formation energy diagrams of Sb_2S_3 under (a) S-rich and (b) S-poor conditions. (c) Transition levels of charged defects in Sb_2S_3 .

impacts the conduction. It is expected that the higher carrier concentration can be achieved in the S-rich condition, although our calculation results suggest that the S vacancies are still likely to form even in the S-rich case.

In summary, we demonstrate the Sb_2S_3 thin film solar cells with 3.8% PCE successfully fabricated using the scalable close space sublimation deposition technique. The microstructure and optical properties of the CSS grown Sb_2S_3 have been characterized experimentally and studied using theoretical approaches. The detailed electronic structure and defect calculations provide insights into the conduction mechanism inside the Sb_2S_3 films, which suggests that the device can be further improved by controlling the S environment during film deposition or through post-deposition sulfurization. Our results show that Sb_2S_3 is suitable for large-scale manufacturing at low cost using CSS-like fast vapor transport technology and it is feasible to integrate Sb_2S_3 into the conventional manufacturing process for thin film solar cells.

See [supplementary material](#) for the lattice parameters and the calculation details of defect formation energy diagram and transition levels of charged defects.

L.P.G. and F.Y. acknowledge the support from the University of Alabama Research Grant Committee fund and the ORAU junior faculty Enhancement Award. B.Z. and X.Q. acknowledge the startup fund from Texas A&M University and the support from Texas A&M Energy Institute.

REFERENCES

- N. M. Haegel, R. Margolis, T. Buonassisi, D. Feldman, A. Froitzheim, R. Garabedian, M. Green, S. Glunz, H.-M. Henning, B. Holder, I. Kaizuka, B. Kroposki, K. Matsubara, S. Niki, K. Sakurai, R. A. Schindler, W. Tumas, E. R. Weber, G. Wilson, M. Woodhouse, and S. Kurtz, *Science* **356**, 141 (2017).
- A. Polman, M. Knight, E. C. Garnett, B. Ehrler, and W. C. Sinke, *Science* **352**, 4424 (2016).
- V. Steinmann, R. E. Brandt, and T. Buonassisi, *Nat. Photonics* **9**, 355 (2015).
- L. Zhang, C. Wu, W. Liu, S. Yang, M. Wang, T. Chen, and C. Zhu, *J. Mater. Chem. A* **6**, 21320 (2018).
- R. Tang, X. Wang, C. Jiang, S. Li, G. Jiang, S. Yang, C. Zhu, and T. Chen, *J. Mater. Chem. A* **6**, 16322 (2018).
- X. Liu, J. Chen, M. Luo, M. Leng, Z. Xia, Y. Zhou, S. Qin, D.-J. Xue, L. Lv, H. Huang, D. Niu, and J. Tang, *ACS Appl. Mater. Interfaces* **6**, 10687 (2014).
- Z. Kai, X. Ding-Jiang, and T. Jiang, *Semicond. Sci. Technol.* **31**, 063001 (2016).
- Y. Zhou, L. Wang, S. Chen, S. Qin, X. Liu, J. Chen, D.-J. Xue, M. Luo, Y. Cao, Y. Cheng, E. H. Sargent, and J. Tang, *Nat. Photonics* **9**, 409 (2015).
- L. Wang, D.-B. Li, K. Li, C. Chen, H.-X. Deng, L. Gao, Y. Zhao, F. Jiang, L. Li, F. Huang, Y. He, H. Song, G. Niu, and J. Tang, *Nat. Energy* **2**, 17046 (2017).
- X. Wen, C. Chen, S. Lu, K. Li, R. Kondrotas, Y. Zhao, W. Chen, L. Gao, C. Wang, J. Zhang, G. Niu, and J. Tang, *Nat. Commun.* **9**, 2179 (2018).
- Q. Ye, Y. F. Xu, W. Y. Chen, S. F. Yang, J. Zhu, and J. Weng, *Appl. Surf. Sci.* **440**, 294 (2018).
- V. Lojpur, J. Krstic, Z. Kacarevic-Popovic, M. Mitric, Z. Rakocevic, and I. L. J. Validzic, *Int. J. Energy Res.* **42**, 843 (2018).
- Y. C. Choi, D. U. Lee, J. H. Noh, E. K. Kim, and S. I. Seok, *Adv. Funct. Mater.* **24**, 3587 (2014).
- L. Guo, B. Zhang, Y. Qin, D. Li, L. Li, X. Qian, and F. Yan, *Sol. RRL* **2**, 1800128 (2018).
- R. Kondrotas, C. Chen, and J. Tang, *Joule* **2**, 857 (2018).
- X. Chen, Z. Q. Li, H. B. Zhu, Y. Wang, B. L. Liang, J. W. Chen, Y. Xua, and Y. H. Mai, *J. Mater. Chem. C* **5**, 9421 (2017).
- C. H. Gao, M. Xu, B. K. Ng, L. L. Kang, L. X. Jiang, Y. Q. Lai, and F. Y. Liu, *Mater. Lett.* **195**, 186 (2017).
- V. Janosevic, M. Mitric, N. Bundaleski, Z. Rakocevic, and I. L. Validzic, *Prog. Photovoltaics Res. Appl.* **24**, 704 (2016).
- H. W. Lei, G. Yang, Y. X. Guo, L. B. Xiong, P. L. Qin, X. Dai, X. L. Zheng, W. J. Ke, H. Tao, Z. Chen, B. R. Li, and G. J. Fang, *Phys. Chem. Chem. Phys.* **18**, 16436 (2016).
- L. Zheng, K. Jiang, J. Huang, Y. Zhang, B. Bao, X. Zhou, H. Wang, B. Guan, L. M. Yang, and Y. Song, *J. Mater. Chem. A* **5**, 4791 (2017).
- D. H. Kim, S. J. Lee, M. S. Park, J. K. Kang, J. H. Heo, S. H. Im, and S. J. Sung, *Nanoscale* **6**, 14549 (2014).
- A. Green Martin, Y. Hishikawa, D. Dunlop Ewan, H. Levi Dean, J. Hohl-Ebinger, and W. Y. Ho-Baillie Anita, *Prog. Photovoltaics Res. Appl.* **26**, 427 (2018).
- G. M. Haket, B. E. McCandless, W. A. Buchanan, S. Fields, and R. W. Birkmire, *J. Vac. Sci. Technol., A* **24**, 1695 (2006).
- D.-B. Li, X. Yin, C. R. Grice, L. Guan, Z. Song, C. Wang, C. Chen, K. Li, A. J. Cimaroli, R. A. Awni, D. Zhao, H. Song, W. Tang, Y. Yan, and J. Tang, *Nano Energy* **49**, 346 (2018).
- P. Hohenberg and W. Kohn, *Phys. Rev.* **136**, B864 (1964).
- W. Kohn and L. J. Sham, *Phys. Rev.* **140**, A1133 (1965).
- G. Kresse and J. Furthmüller, *Phys. Rev. B* **54**, 11169 (1996).
- J. P. Perdew, K. Burke, and M. Ernzerhof, *Phys. Rev. Lett.* **77**, 3865 (1996).
- D. C. Langreth and M. J. Mehl, *Phys. Rev. B* **28**, 1809 (1983).
- M. Dion, H. Rydberg, E. Schröder, D. C. Langreth, and B. I. Lundqvist, *Phys. Rev. Lett.* **92**, 246401 (2004).
- G. Román-Pérez and J. M. Soler, *Phys. Rev. Lett.* **103**, 096102 (2009).
- J. Klimeš, D. R. Bowler, and A. Michaelides, *Phys. Rev. B* **83**, 195131 (2011).
- H. J. Monkhorst and J. D. Pack, *Phys. Rev. B* **13**, 5188 (1976).
- A. D. Becke and E. R. Johnson, *J. Chem. Phys.* **124**, 174104 (2006).
- A. V. Krukau, O. A. Vydrov, A. F. Izmaylov, and G. E. Scuseria, *J. Chem. Phys.* **125**, 224106 (2006).
- C. Freysoldt, J. Neugebauer, and C. G. Van de Walle, *Phys. Rev. Lett.* **102**, 016402 (2009).
- Y. Kumagai and F. Oba, *Phys. Rev. B* **89**, 195205 (2014).
- S. J. Yuan, H. Deng, X. K. Yang, C. Hu, J. Khan, W. N. Ye, J. Tang, and H. S. Song, *ACS Photonics* **4**, 2862 (2017).
- M. A. Contreras, M. J. Romero, B. To, F. Hasoon, R. Noufi, S. Ward, and K. Ramanathan, *Thin Solid Films* **403-404**, 204 (2002).
- P. Makreski, G. Petruševski, S. Ugarković, and G. Jovanovski, *Vib. Spectrosc.* **68**, 177 (2013).
- C. Pilapong, T. Thongtem, and S. Thongtem, *J. Alloys Compd* **507**, L38 (2010).
- M. Zhong, X. Wang, S. Liu, B. Li, L. Huang, Y. Cui, J. Li, and Z. Wei, *Nanoscale* **9**, 12364 (2017).
- X. Liu, X. Xiao, Y. Yang, D.-J. Xue, D.-B. Li, C. Chen, S. Lu, L. Gao, Y. He, M. C. Beard, G. Wang, S. Chen, and J. Tang, *Prog. Photovoltaics Res. Appl.* **25**, 861 (2017).